

Reliability of charge carrier recombination data determined with charge extraction methods

Cite as: J. Appl. Phys. 126, 205501 (2019); doi: 10.1063/1.5129037

Submitted: 27 September 2019 · Accepted: 4 November 2019 ·

Published Online: 25 November 2019



Juliane Kniepert,¹ Andreas Paulke,¹ Lorena Perdigón-Toro,¹ Jona Kurpiers,¹ Huotian Zhang,² Feng Gao,² Jun Yuan,³ Yingping Zou,³ Vincent M. Le Corre,⁴ L. Jan Anton Koster,^{4,a)} and Dieter Neher^{1,b)}

AFFILIATIONS

¹Institute of Physics and Astronomy, University of Potsdam, Karl-Liebknecht-Str. 24-25, 14476 Potsdam-Golm, Germany

²Department of Physics, Chemistry and Biology (IFM), Linköping University, 581 83 Linköping, Sweden

³College of Chemistry and Chemical Engineering, Central South University, Changsha 410083, People's Republic of China

⁴Photophysics and Optoelectronics, Zernike Institute for Advanced Materials, Nijenborgh 4, NL-9747AG Groningen, The Netherlands

^{a)}Electronic mail: l.j.a.koster@rug.nl

^{b)}Electronic mail: neher@uni-potsdam.de

ABSTRACT

Charge extraction methods are popular for measuring the charge carrier density in thin film organic solar cells and to draw conclusions about the order and coefficient of nongeminate charge recombination. However, results from such studies may be falsified by inhomogeneous steady state carrier profiles or surface recombination. Here, we present a detailed drift-diffusion study of two charge extraction methods, bias-assisted charge extraction (BACE) and time-delayed collection field (TDCF). Simulations are performed over a wide range of the relevant parameters. Our simulations reveal that both charge extraction methods provide reliable information about the recombination order and coefficient if the measurements are performed under appropriate conditions. However, results from BACE measurements may be easily affected by surface recombination, in particular for small active layer thicknesses and low illumination densities. TDCF, on the other hand, is more robust against surface recombination due to its transient nature but also because it allows for a homogeneous high carrier density to be inserted into the active layer. Therefore, TDCF is capable to provide meaningful information on the order and coefficient of recombination even if the model conditions are not exactly fulfilled. We demonstrate this for an only 100 nm thick layer of a highly efficient nonfullerene acceptor (NFA) blend, comprising the donor polymer PM6 and the NFA Y6. TDCF measurements were performed as a function of delay time for different laser fluences and bias conditions. The full set of data could be consistently fitted by a strict second order recombination process, with a bias- and fluence-independent bimolecular recombination coefficient $k_2 = 1.7 \times 10^{-17} \text{ m}^3 \text{ s}^{-1}$. BACE measurements performed on the very same layer yielded the identical result, despite the very different excitation conditions. This proves that recombination in this blend is mostly through processes in the bulk and that surface recombination is of minor importance despite the small active layer thickness.

Published under license by AIP Publishing. <https://doi.org/10.1063/1.5129037>

I. INTRODUCTION

The field of organic solar cells (OSCs) has seen tremendous progress in the last 15 years and is now on the verge of commercial application with certified power conversion efficiencies (PCEs) exceeding 15% for single junction structures.^{1–3} Despite this success, current PCEs are still far below the theoretical Shockley-Queisser limit, issuing an ongoing challenge to the OSC research community. One key parameter limiting the performance is the

nongeminate recombination (NGR) of photogenerated charge carriers in the active medium. In organic solar cells, free carrier recombination is mostly through bimolecular recombination (BMR),⁴ implying that the carrier lifetime is a strong function of the carrier density. As a consequence, the fill factor is depending on the generation rate, the bimolecular recombination coefficient, the layer thickness, and the carrier mobilities.^{5–8} As such, BMR sets a limit to the optimum layer thickness of the absorber layer.⁹

In particular for blends with efficient charge generation, thin active layers are often chosen in order to extract photogenerated charge carriers before they recombine in the bulk. Yet, thin layers mean a loss of the overall absorption of light and generation of free charges, which limits the output current of the device. On the other hand, while BMR is a second order process, the presence of traps and recombination of minority carriers at the electrode (surface recombination) lead to additional first order recombination channels. To further push the efficiency of OSC, it is a crucial task to identify and quantify recombination processes in operational devices under relevant conditions and at the relevant times scales—from nanoseconds to steady state.

In the past, time-resolved transient absorption spectroscopy (TAS) has been one of the most frequently employed techniques to measure charge carrier decay dynamics and rate coefficients.^{10–12} However, only a few studies were made on complete devices¹³ and, in general, TAS requires high fluences, beyond the regime relevant to photovoltaics, to obtain reasonable signal-to-noise ratios. Likewise, this technique does not deliver steady state recombination data. The method of photogenerated charge extraction by linearly increasing voltage (photo-CELIV) is well suited to perform recombination measurements at low fluences and carrier densities,^{14,15} but it lacks the time resolution to capture early time recombination. Alternatively, small perturbation optoelectronic measurements based on transient photovoltage (TPV) are conducted on devices under relevant working conditions.^{16–18} However, it was pointed out recently that lifetimes obtained by TPV on thin film devices may be influenced by capacitive contributions.^{19,20}

An indirect way to study the order and coefficient of recombination is to determine the charge carrier density in the device as a function of illumination intensity (and bias) and connect it with the recombination current under the same conditions. Popular methods are charge extraction (CE),²¹ differential charging (DC),¹⁶ or impedance spectroscopy (IS).²² It has, however, been noted that in devices under steady state operating conditions, charge carrier profiles can be highly inhomogeneous because of dark injection from the electrodes.^{20,23–25} The effect is most pronounced for thin active layers and low illumination conditions (low excess carrier density). As a result, the extracted carrier density from CE, which is the drift-length weighted average of the charge carrier distribution (see below), may differ largely from the mean density, leading to, e.g., an apparent higher order of mobility.^{24,25} However, even if the average charge density is determined correctly (e.g., via DC), an inhomogeneous carrier profile will cause the recombination rate to vary across the active layer, meaning that the analysis of total recombination current in combination with the spatially averaged carrier densities may not give the true (local) recombination order and coefficient.²³ The situation becomes even more complicated in the presence of surface recombination. In this case, photogenerated carriers exit the device at the wrong contact (electrons at the anode or holes at the cathode) due to poor contact selectivity. As a result, the carrier density profile becomes highly inhomogeneous,²⁶ but also the extra surface recombination current (being linear in the minority carrier density at the respective contact) may mask the nature of the bulk recombination process.²⁴

Recently, we have reported on two complementary techniques to measure the recombination order and coefficients, namely,

time-delayed collection field (TDCF)²⁷ and bias-assisted charge extraction (BACE).²⁸ Although both methods are based on the extraction of photogenerated charge carriers upon application of a reverse bias voltage, there are distinctive differences in the measurement conditions and the physical concepts behind the data analysis. In TDCF, charge carriers are generated with a short (nanosecond) laser pulse and subsequently extracted with a high reverse bias (collection bias V_{coll}) after a variable delay time. During generation and delay, the device is held at a given prebias (V_{pre}) close to V_{OC} , e.g., at the maximum power point. The delay between the laser pulse and the extraction pulse allows recombination to evolve for a well-defined time period. The analysis of the extracted charge (Q_{pre}) during prebias and the extracted charge (Q_{coll}) during application of the collection bias yields information on how the charges move and recombine.

In contrast, in a BACE experiment, the device is illuminated with a steady state light source of defined intensity while being held at a constant bias that corresponds exactly to the V_{OC} at that intensity. In good approximation, the net current density at each point in the bulk is zero and the rates of generation and recombination are equal. When switching off the light source, the external bias is rapidly changed to the reverse direction. Integration of the photocurrent transient then yields the amount of mobile charge that was present in the device under illumination. Analysis of the carrier density at different illumination intensities as a function of generation rate reveals information on the dominant recombination order and coefficient.

Both techniques have been extensively used to examine time-dependent and steady state recombination properties for a wide range of materials, revealing important information on the rate and order of recombination.^{29–34} The accuracy of these results was confirmed by drift-diffusion simulations of the transient and steady state photocurrents.^{28,35} However, the analysis of the TDCF and BACE photocurrent data relies on a number of simplified assumptions. The most critical one is that the spatial distribution of the charge carriers is assumed to be uniform across the layer before extraction. Only in this case does every charge carrier travel in average half the layer thickness and the integral over time corresponds exactly to the total carrier density in the device. To take injected dark charge into account in the analysis of the TDCF experiments, an additional background charge is included, which, for simplification, is assumed to be homogeneous in the layer.²⁸ However, the true distribution of the background charge depends on layer thickness, external bias, and injection barriers, and might in fact be very inhomogeneous. This raises the question on how the background charge influences the charge carrier dynamics in the TDCF experiment and how it can be accounted for.

In this paper, we use one dimensional drift-diffusion simulations to study charge extraction under realistic conditions, i.e., taking into account the injection of charges from the electrodes and resulting inhomogeneous charge carrier profiles. In particular, we investigate the influence of recombination coefficients, layer thickness, illumination intensity, and bias on the outcome of TDCF and BACE measurements. A particular focus is on the influence of surface recombination on the results from BACE and TDCF. It turns out that both methods work surprisingly well even if the simplified assumptions are not fulfilled. We identify the parameter range and conditions that lead to reliable results and point out conditions where special care is necessary.

II. METHODS

1D drift-diffusion simulations: Numerical drift-diffusion simulations of the carrier densities under steady state illumination and in the dark were performed with a code published in Ref. 36. The kinetic TDCF simulations were performed using a transient drift-diffusion simulation tool as described in Refs. 37 and 38, following closely the experimental measurement scheme. At first, the device is held for a sufficient time in equilibrium in the dark at a certain prebias, which allows establishing a steady state background charge distribution in the device. The injection barriers in all simulations were set to 0.1 eV, and the contacts are assumed to be in thermodynamic equilibrium where the Boltzmann statistics are used to determine the carrier densities at the first and last grid point of the device. At $t = 0$, an additional homogeneous charge carrier density is instantaneously inserted in the layer, imitating the laser pulse in the measurement. The additional charge carriers may then either leave the device or recombine with each other or with the dark carriers. Recombination between any charge carriers is implemented as a bimolecular process with a constant BMR coefficient k_2 . After the time delay, a high reverse bias (V_{coll}) is applied to rapidly collect all remaining charge carriers from the device. The motion of the charge carriers results in an electrical current I_{ext} in the external circuit, through a measurement resistor R . Like in the real experiment, the same voltage jump is also performed without illumination to account for capacitive charging. The difference between the currents with and without the laser pulse yields the photocurrent I_{photo} of the photogenerated excess charge carriers. Notably, if dark charge is present, this voltage jump in the dark will also account for the drift-length weighted dark charge distribution. For each delay time, the photocurrent transients are integrated to yield the extracted precharge: $Q_{\text{pre}}(t_d) = \int_0^{t_d} I_{\text{photo}} dt$, the charge present in the device at t_d : $Q_{\text{coll}}(t_d) = \int_{t_d}^{t_{\text{max}}} I_{\text{photo}} dt$, and the total charge: $Q_{\text{tot}}(t_d) = \int_0^{t_{\text{max}}} I_{\text{photo}} dt$; the latter being the photogenerated charge surviving charge recombination. Here, t_{max} is the total time of the extraction pulse. Dividing Q by the active sample volume yields the carrier density n . From these data, the recombination rate R is calculated via $R(t_d) = (n_{\text{tot}}(t_d + \Delta t) - n_{\text{tot}}(t_d))/\Delta t$, where Δt is the time increment in the simulation. To construct the differential decay plots, $R(t_d)$ is plotted vs n_{coll} , where the latter is represented by its average value $(n_{\text{coll}}(t_d + \Delta t) + n_{\text{coll}}(t_d))/2$ in the considered time increment.

Device preparation: The polymer PM6 was purchased from Solarmer Materials Inc. The small acceptor molecule Y6 was synthesized according to the literature.¹ The solvents chloroform (CHCl_3) and the additive chloronaphthalene (CN) were purchased from Carl Roth and Alfa Aesar, respectively. The devices were fabricated with a structure ITO/ZnO/PM6:Y6/MoO_x/Ag. Patterned ITO (Lumtec) substrates were cleaned in an ultrasonic bath with acetone, Hellmanex, deionized water, and isopropanol for 10 min, followed by microwave plasma treatment (4 min at 200 W). Subsequently, ZnO nanoparticles (Avantama N-10) dissolved in isopropanol were filtered through a 0.45 μm polytetrafluoroethylene (PTFE) filter and spin coated onto ITO at 4000 rpm under ambient conditions. The ZnO substrates were thermally annealed at 120 °C for 30 min, followed by exposition to UV light inside a

nitrogen-filled glovebox for 10 min. PM6 and Y6 were dissolved in CHCl_3 to a total concentration of 16 mg ml^{-1} with a 1 to 1.2 weight ratio and 0.5% CN (v/v, CN/ CHCl_3) as additive. The solution was stirred for 3 h inside the glovebox. Then, the blend was spin coated (2500–3000 rpm) onto the ZnO layer to obtain a photoactive layer of thickness ~ 100 nm. To complete the devices, 10 nm of MoO_x as the anode interlayer and 100 nm of Ag as the top electrode were evaporated under a 10^{-6} – 10^{-7} mbar vacuum. The resulting active area was 0.55 or 1.1 mm^2 for TDCF and BACE experiments. This device had a power conversion efficiency of 13.5%. Details about the optoelectronic properties of the device including the efficiency of charge generation will be published elsewhere.

Time-delayed collection field (TDCF): In TDCF, the device was excited with a laser pulse from a diode pumped, Q-switched Nd:YAG laser (NT242, EKSPLA) with ~ 5 ns pulse duration at a typical repetition rate of 500 Hz. To compensate for the internal latency of the pulse generator, the laser pulse was delayed and homogeneously scattered in an 85 m long silica fiber (LEONI). Then, charges were generated while the device was held at different prebias V_{pre} . After a preset delay time, a reverse bias, $V_{\text{coll}} = -2.5$ V, was applied to extract all the charges in the device. V_{pre} and V_{coll} were set by an Agilent 81150A pulse generator through a home-built amplifier, which was triggered by a fast photodiode (EOT, ET-2030TTL). The current flowing through the device was measured via a 10 Ω resistor in series with the sample and recorded with an oscilloscope (Agilent DSO9104H). Great care was taken to avoid free carrier recombination prior to extraction. Therefore, a fast ramp-up (~ 2.5 ns) of the bias was applied.

Bias-assisted charge extraction (BACE): The experimental setup for BACE is similar to that of TDCF but changing primarily the illumination conditions. To establish steady state conditions, we used a high power 1 W, 638 nm laser diode (insaneware) with a switch-off time of ~ 10 ns. The laser diode was operated at 500 Hz with a duty cycle of 50%, such that illumination lasted 1 ms and the diode was switched off for also 1 ms. Right after switching off the laser, a high reverse bias was applied to the sample by the same fast pulse generator (Agilent 81150A) as in TDCF measurements, allowing a fast extraction time of 10–20 ns. The current transients were measured via a 10 Ω resistor in series with the sample and recorded with an oscilloscope (Agilent DSO9104H).

III. RESULTS FROM DRIFT-DIFFUSION SIMULATIONS

It has been shown that in devices under steady state illumination and bias conditions, the distribution of charge carriers is rather inhomogeneous.^{23,24} In particular, if the injection barriers are low, the charge carrier densities near the contacts may be very high, possibly several orders of magnitude higher than in the bulk.³⁹ Figure 1(a) shows simulated carrier density profiles at open circuit conditions for a typical device of 100 nm with injection barriers of $\phi_{\text{B}} = 0.1$ eV and assuming infinite surface recombination velocities at both contacts. The simulated generation rate was $G = 5 \times 10^{27} \text{ m}^{-3} \text{ s}^{-1}$, the BMR coefficient was set to $k_2 = 1 \times 10^{-17} \text{ m}^3 \text{ s}^{-1}$, and electron and hole mobilities were $\mu_e = \mu_h = 1 \times 10^{-3} \text{ cm}^2 \text{ V}^{-1} \text{ s}^{-1}$. The simulation used here is based on a drift-diffusion model where nongeminate recombination is implemented as a bimolecular process.³⁶ At the steady state, the carrier

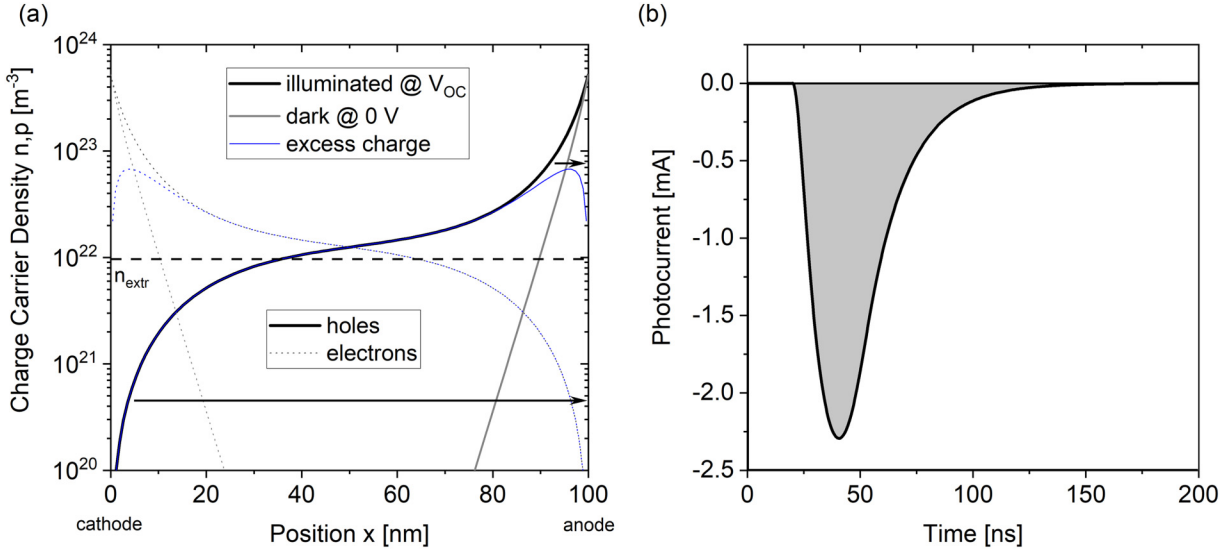


FIG. 1. (a) Simulated charge carrier density profiles for a 100 nm device under illumination at $V_{OC} = 0.705$ V with injection barriers of 0.1 eV, a generation rate of $G = 5 \times 10^{27} \text{ m}^{-3} \text{ s}^{-1}$, a BMR coefficient of $k_2 = 1 \times 10^{-17} \text{ m}^3 \text{ s}^{-1}$, and electron and hole mobilities of $\mu = 1 \times 10^{-3} \text{ cm}^2 \text{ V}^{-1} \text{ s}^{-1}$. The surface recombination velocity was set to infinite at both contacts. In the absence of electrodes, the generation-recombination balance would establish a steady state carrier density $n_e = n_h = 2.2 \times 10^{22} \text{ m}^{-3}$. Under reverse bias, electrons move to the cathode ($x = 0$) and holes to the anode ($x = d$). As indicated by the arrows, a large amount of charge travels a short distance to the electrode, while only a few charge carriers move through the whole layer thickness. Therefore, the extracted carrier density n_{extr} [see Eq. (2)] is smaller than predicted from the simply generation-recombination balance. (b) Simulated transient under the assumption that all holes from the device in (a) are extracted at the anode with an extraction voltage of -5 V. The large reverse bias leads to rapid extraction of charges.

distribution in the device is then established by a combination of photogeneration, recombination, injection, and extraction of charge carriers. Especially at low illumination levels and low layer thicknesses, the injected charge carriers dominate the distribution in the device.

In a charge extraction experiment, the carrier density is determined from the integral of the extraction current transient over time, as shown in Fig. 1(b). Charge extraction from thin layers of intrinsic semiconductors has been treated in several publications.^{20,40} In short, let us consider a positive charge Q , situated at position x in a semiconductor layer of thickness d and permittivity $\epsilon = \epsilon_0 \epsilon_r$, sandwiched between a cathode at $x = 0$ and an anode at $x = d$. According to Poisson's equation, when this charge is moved to the anode, the electrostatic potential of the anode (relative to the cathode) increases by $\Delta V = \frac{Q/A}{\epsilon} (d - x) = \frac{Q}{C_g} \frac{d-x}{d}$, where A is the area and C_g is the geometric capacity of the device. If the external bias is kept constant, this causes a current in the external circuit to compensate the potential change due to charge displacement. The integral of this external current gives what we measure as the extracted charge: $Q_{extr} = C_g \Delta V = Q \frac{d-x}{d}$. Therefore, $Q_{extr} < Q$, except for the case where the charge travels through the entire layer during extraction. If now $n_h(x)$ is the hole density profile in the moment when the extraction starts, complete extraction of all holes to the anode causes an extracted charge of

$$Q_{h,extr} = \frac{eA}{d} \int_0^d (d-x) \cdot n_h(x) dx \equiv (eAd) n_{h,extr}. \quad (1)$$

Therefore, the extracted hole density can be written as

$$n_{h,extr} = \bar{n}_h \cdot \frac{(d - \bar{x}_h)}{d}, \quad (2a)$$

where $\bar{n}_h = \frac{1}{d} \int_0^d n_h(x) dx$ is the spatially averaged hole density and $\bar{x}_h = \frac{\int_0^d x \cdot n_h(x) dx}{\int_0^d n_h(x) dx}$ is the mean position of the hole distribution.

For electrons extracted at the cathode at $x = 0$,

$$n_{e,extr} = \bar{n}_e \cdot \frac{\bar{x}_e}{d}. \quad (2b)$$

Therefore, the extracted carrier density is determined by the average carrier density and the average distance traveled by each carrier during extraction. In the case of the carrier distribution shown in Fig. 1(a), there are many charge carriers close to the extracting electrode that travel only a small distance and only a few charge carriers at the opposite electrode that travel the whole distance. Therefore, $n_{extr} < \bar{n}$. Also, even if the average electron and hole density is the same, the average drift length may differ largely for the two types of carriers, leading to $n_{e,extr} \neq n_{h,extr}$. Only when electrons and holes are homogeneously distributed and their densities are equal,

$$n_{extr} = n_{e,extr} + n_{h,extr} = \frac{1}{2} n_e + \frac{1}{2} n_h \cong n_e = n_h = n. \quad (2c)$$

Though this condition is generally not fulfilled, the analysis of data from extraction experiments relies on the assumption that the extracted carrier density is equal to the average electron resp. hole density. The same is actually true in impedance spectroscopy, where it is assumed that the extra charge $dQ = CdV$, which is injected into the device upon a small voltage increase dV , distributes homogeneously across the active volume. In addition, BACE as well as TDCF measurements always include the correction by a dark reference pulse, starting at 0 V or V_{pre} , respectively, and using the same voltage step to negate capacitance effects. We show below that such dark carrier densities are generally inhomogeneously distributed throughout the active layer. We call the carrier density out of the BACE or TDCF measurement that is corrected by the dark reference measurement at 0 V the excess carrier density n_{exc} . This is the physical quantity accessible in the experiments.

A. Bias-assisted charge extraction (BACE)

Having introduced the important physical quantities, we now turn to the analysis of recombination coefficient and order using the bias-assisted charge extraction (BACE) method. In a BACE measurement, the device is illuminated with a steady state light source with varying intensities while being held at a constant bias equal to the V_{OC} at that intensity. The V_{OC} and short circuit current (J_{SC}) of the device have been measured in advance for each particular light intensity. Assuming that under short circuit conditions all charge carriers are extracted, the charge carrier generation rate G can be determined from the J_{SC} according to $G = J_{SC}/ed$, where e is the elementary charge and d is the device thickness. In

general, J_{SC} conditions are not sufficient to extract all charge carriers. In this case, the current density at a higher reverse bias is used to determine the generation rate.²⁸

The integrated carrier densities from the BACE current transients are then plotted against the generation rates. Under the assumption that the net current density at each point in the bulk was zero, the rates of generation and recombination (R) are equal and the slope of the log-log plot of G vs n corresponds to the recombination order δ according to

$$G = R = k_{\delta} n^{\delta}. \quad (3)$$

Here, k_{δ} is a general recombination coefficient. In the case of bimolecular recombination (BMR), $\delta = 2$ and k_{δ} becomes the BMR coefficient k_2 , which can be calculated using Eq. (3).

Our simulations follow exactly the measurement scheme. For a given device characterized by layer thickness, BMR coefficient, charge carrier mobilities, and contact properties, J - V curves for different applied generation rates are simulated to obtain $V_{OC}(G)$. In the next step, the charge carrier density profile at V_{OC} is simulated from which the extractable carrier density is determined with Eqs. (1) and (2). In the following, we perform BACE simulations with different layer thicknesses, BMR coefficients, and contact properties (i.e., zero or infinite surface recombination), to define a parameter range where reliable results can be obtained.

Figure 2(a) shows the results for two layer thicknesses (100 nm and 250 nm) and three different BMR coefficients ($k_2 = 10^{-16}$, 10^{-17} , and $10^{-18} \text{ m}^3 \text{ s}^{-1}$). Here, the surface recombination was set to zero for both contacts. The dashed lines indicate the

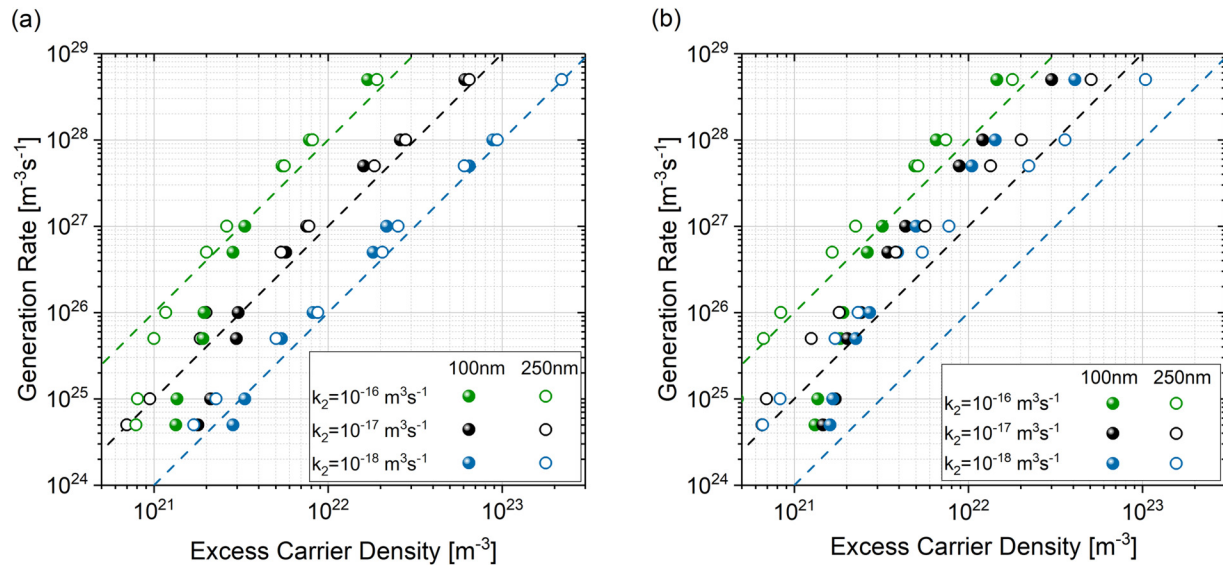


FIG. 2. (a) Simulated excess carrier density (dots), calculated according to Eq. (2) and corrected for the dark charge from the reference measurement at 0 V, as a function of the generation rate for different layer thicknesses and BMR coefficients. Surface recombination at both contacts was set to 0. (b) As in (a), except that here, the surface recombination was set to infinity at both contacts. In both graphs, the electron and hole mobility was $\mu = 1 \times 10^{-3} \text{ cm}^2 \text{ V}^{-1} \text{ s}^{-1}$ and injection barrier was 0.1 eV at both contacts. The dashed lines indicate the carrier density according to $G = R = k_2 n^2$ for each respective BMR coefficient, which serves as an "electrodeless" reference for the simulated values (dots).

theoretical dependence of carrier density on generation rate for the three BMR coefficients. It is obvious that in the absence of surface recombination, in all cases the results from our analysis correspond well to the input value of k_2 , except for very low charge carrier densities. For high enough carrier densities in the bulk, the charge carrier density profiles become fairly homogeneous, and the drift-length weighted carrier density approaches the bulk carrier density. Example carrier density profiles for different generation rates and layer thicknesses are shown in the [supplementary material](#) (Fig. S1). It becomes clear that for low generation rates the density profiles are very inhomogeneous as they are dominated by the injected charge in the space charge regions close to the contacts. In this case, the extracted carrier density becomes almost independent of the generation rate and the $G(n)$ plot reveals a slope that is greater than 2. This would suggest a recombination order higher than 2; however, as our simulations clearly show, this deviation is the result of an inhomogeneous carrier distribution. For the 250 nm device, we find a slope of 2 also for lower carrier densities down to approximately $1 \times 10^{21} \text{ m}^{-3}$. This is because the space charge regions become less important compared to the bulk for larger layer thicknesses and the density profiles are homogeneous also for lower generation rates.

Recombination orders higher than 2 have been frequently reported in the literature.^{17,35,41} In some cases, this phenomenon has been interpreted as BMR with $k_2(n)$ being dependent on carrier density. While the participation of more than two particles in a recombination process is quite unlikely, it cannot be ruled out that k_2 is a function of n if, for instance, the mobilities are carrier density dependent.⁴¹ Likewise, recombination among carriers which occupy a broad density of states distribution may be the reason of an apparent higher recombination order.⁴² Experimental conditions should be carefully examined and reviewed to exclude measurement artifacts. Our general advice is to work at charge carrier densities greater than $5 \times 10^{21} \text{ m}^{-3}$ to be on the safe side and with layer thicknesses as large as possible for a certain material combination. The exact values for illumination intensity and layer thickness also depend on the injection barriers and recombination coefficient. In general, the lower the injection barriers, the more inhomogeneous will be the carrier density profile as the injected charge at the contacts largely dominates the spatial distribution. Therefore, larger layer thicknesses should be used and higher illumination intensities are necessary to achieve reliable measurement conditions. For the recombination coefficient, the opposite tendency is true. The faster the recombination, the higher is the required illumination intensity to reach the same bulk carrier density. Therefore, the recombination coefficient is implicitly accounted for the correct choice of the carrier density range. We finally note that according to Fig. 2, BACE has the tendency to overestimate the recombination coefficient for relevant carrier densities of 10^{22} – 10^{23} m^{-3} (the simulated data lie above the exact rate). This is in part due to the fact that under steady state illumination, the carrier density profile is never homogeneous: due to recombination with dark charge, the photogenerated hole (electron) density is diminished at the cathode (anode).

Figure 2(b) shows the simulation results for the same parameters as in Fig. 2(a), except here the surface recombination was set to infinity for both contacts. Now, the agreement between theory and

simulation is worse for all parameters. In general, the simulated carrier density in the device is lower (and, therefore, the apparent k_2 is higher) than expected because a significant amount of charge carriers are lost at the contacts due to surface recombination. This also lowers the carrier density in the bulk due to diffusion. The charge carrier density profiles with and without surface recombination can be found in the [supplementary material](#) (Fig. S1). Only for the highest bulk recombination coefficient, reasonable agreement is found since in this case bulk recombination still dominates over surface recombination, which means the losses at the contacts are less severe and the carrier density probed by BACE is mainly determined by bimolecular recombination.

Interestingly, none of the cases presented in Fig. 2(b) display a recombination order of one, which would be expected especially for dominant surface recombination (low BMR coefficients = insignificant bulk recombination). Our simulations show instead that a slope of one is only observed for very high carrier densities, which cannot be achieved in realistic experiments. The reason for the higher recombination order at low to intermediate carrier densities may lie in the used contact energetics, where we set the injection barriers in all simulations to be 0.1 eV only. Sandberg *et al.* simulated the effect of surface recombination for the case of small (ohmic contacts) and large (nonohmic contacts) injection barriers.⁴³ In the former case, band bending within the organic semiconductor creates an energetic barrier for carriers to reach the “wrong contact,” and this barrier will be dependent on the carrier density (quasi-Fermi-level splitting) in the bulk. As a consequence, the surface recombination current becomes a superlinear (in the limit of dominant surface recombination strictly quadratic) function of the bulk carrier density [see Eqs. (14) and (16) in Ref. 43], exactly what we are seeing here. Therefore, if steady state recombination measurements reveal a second order dependence of the recombination rate, this does not necessarily mean that it is dominated by free carrier encounter in the bulk.

As expected, the extracted values of k_2 are closer to the input parameter when going to higher layer thicknesses (250 nm, empty circles), as for thicker devices losses at the contacts become less important for the carrier density in the bulk. However, for the lowest recombination coefficient, k_2 taken out of the simulations is still up to one order of magnitude too high and the slope in the log-log plot is smaller than two. Only for the highest recombination coefficient, BACE reproduces the order and the input values of k_2 well.

In summary, in the case of infinite surface recombination, no reliable results regarding the recombination order and coefficient can be obtained from a BACE experiment. Only for very high BMR, carrier densities and layer thicknesses does the bulk recombination dominate over losses at the contacts and the values obtained with BACE are correct. For intermediate and low BMR, the contact losses are predominant and this changes the apparent recombination coefficient and order measured with BACE. However, in a single experiment it cannot be distinguished whether surface recombination is present or not. To exclude the case of infinite surface recombination, BACE experiments should be performed at various layer thicknesses. Only if all curves for all layer thicknesses fall on one line, reliable results can be expected.

B. Time-delayed collection field (TDCF)

In the following, we discuss the analysis of recombination order and coefficients in time-delayed collection field (TDCF) measurements with special emphasis on the range of validity. A detailed description of the measurement scheme and experimental setup can be found elsewhere.⁴⁴ In TDCF, the charge carriers are generated with a short laser pulse at $t=0$ and, after a variable delay time, extracted with a high reverse bias. As described in Sec. II, the current transients are integrated over time to yield the density of photogenerated charge carriers exiting the device before the extraction voltage is applied, $n_{pre}(t_{del})$, and the photogenerated carrier density being present in the device at the delay time, $n_{coll}(t_{del})$. Then, $n_{tot}(t_{del}) = n_{pre}(t_{del}) + n_{coll}(t_{del})$ is the total extracted charge carrier density, which is the carrier density that survived recombination for a given t_{del} . Note that as in a real TDCF experiment, measured carrier densities are corrected for the corresponding dark values, which are gained from TDCF measurement in the dark on the same device and under the same bias conditions.

In contrast to BACE, which relies on the steady state carrier distribution, the initial density profile of photogenerated electrons and holes is the same, though it might vary spatially depending on the absorption of the active material and cavity effects. In the ideal case, with a homogeneous carrier distribution and no dark-injected charge, the fate of the photogenerated carrier population is given by a simple second order process with a bimolecular recombination coefficient k_2 : $\frac{dn_{tot}}{dt} = -k_2 n_{coll}^2$. Importantly, during the delay the device is usually held at a forward bias close to flat band conditions in order to reduce the internal electric field. Under these conditions, a considerable density of background charge (n_{BG}) due to dark injection from the contacts is expected to be present in the device before the laser pulse, also taking part in the recombination process with the photogenerated carriers. A simplistic model describing this situation has been developed earlier in this group,^{28,31}

$$\frac{dn_{tot}}{dt} = -k_2(n_{coll}^2 + 2n_{coll}n_{BG}). \quad (4)$$

Therefore, the decay of n_{tot} with increasing t_{del} is no more a simply quadratic function of n_{coll} . In order to determine how the recombination process depends on the carrier density, the recombination rate $R(t_d) = (n_{tot}(t_d + \Delta t) - n_{tot}(t_d))/\Delta t$ is plotted vs n_{coll} on a double logarithmic scale. Then, the apparent recombination order at a given time delay is read off from the slope δ of the curve. According to this model, for high carrier densities (i.e., high pulse fluences) recombination between photogenerated charge carriers is dominating, leading to a slope of 2, while for low carrier densities, bimolecular recombination with the background charge is dominating, leading to a slope of 1 in the log-log plot. By fitting the experimental data with Eq. (4) and leaving k_2 and n_{BG} as free fit parameters, the model can be used to extract the recombination coefficient and the effective background charge from the TDCF data.

The derivation of Eq. (4) is based on a number of simplifying assumptions. First of all, the background carrier density is assumed to be distributed homogeneously across the layer at the time the photogenerated carriers are inserted. This is probably the most

critical point of the model, as the dark carrier profile is governed by the injection, diffusion, and recombination. Depending on the exact prebias, layer thickness, and height of injection barriers, the background charge might in fact become very inhomogeneous.

Second, it is assumed that recombination is absent during collection and all remaining charge carriers after the delay can be extracted. This approximation might be true for low recombination constants. However, for fast or even dispersive recombination dynamics, losses of charge carriers during extraction cannot be excluded. Last but not least, the model assumes that surface recombination at the contacts is zero, i.e., minority carriers may not leave the device at the “wrong” electrode. It is not clear how the TDCF data are affected, if surface recombination at both contacts would be present.

Therefore, numerical simulations have been performed with different prebias and recombination constants to examine, under controlled conditions, how the dark charge distribution and recombination during extraction will affect the data analysis and whether the model is able to produce correct results even if the simplified assumptions are not fulfilled. Finally, the influence of surface recombination on the TDCF data is carefully investigated for different layer thicknesses.

Figure 3 shows the results of the TDCF simulations for a 100 nm device with zero surface recombination at the contacts, electron and hole mobilities of $\mu = 1 \times 10^{-3} \text{ cm}^2 \text{ V}^{-1} \text{ s}^{-1}$, and a BMR coefficient of $k_2 = 1 \times 10^{-17} \text{ m}^3 \text{ s}^{-1}$. The simulations were performed at a prebias of 0.7 V, which is close to the open circuit voltage at one sun for the considered device ($V_{OC} = 0.74 \text{ V}$ at $G = 4 \times 10^{27} \text{ m}^{-3} \text{ s}^{-1}$ with an effective bandgap of 1.1 eV and an effective DOS of $2.5 \times 10^{25} \text{ m}^{-3}$). Figure 3(a) displays the temporal evolution of the total carrier density n_{tot} (as a function of the time delay) for different initial carrier densities (representing different laser pulse fluences in the measurement). Note that each data point in the graph corresponds to the integral of a simulated TDCF transient. From this graph, it is obvious that the temporal decay of the carrier density is more pronounced for higher initial carrier densities. This is expected for a BMR process as it is implemented in the simulation. In Fig. 3(b), n_{tot} (full circles) and n_{pre} (open circles) are shown, normalized to n_{tot} at a delay of 5 ns. The colors of the data points correspond to the initial carrier densities shown in Fig. 3(a) with dark blue being the lowest and dark orange being the highest initial carrier density. Increasing the delay results in a continuous increase of n_{pre} as more and more charges leave the device prior to the application of the collection pulse. At the same time n_{tot} , being the initially photogenerated charge carrier density reduced by all recombination losses during the delay, exhibits a continuous drop. Finally, in Fig. 3(c), the differential change of the total carrier density dn_{tot}/dt is plotted vs n_{coll} on a double logarithmic scale. The data points for all delays and fluences [the same color code as in Figs. 3(a) and 3(b) is used] are lying on one line. This result seems to be expected as the simulation was carried out with a time-independent recombination coefficient. However, as V_{pre} was selected to be smaller than V_{OC} , charge displacement is occurring during the delay, not only reducing the carrier density but also rendering the remaining charge carrier profile more and more inhomogeneous. Still, at high carrier densities, the rapid build-up of space charge prevents further extraction and leads to rather

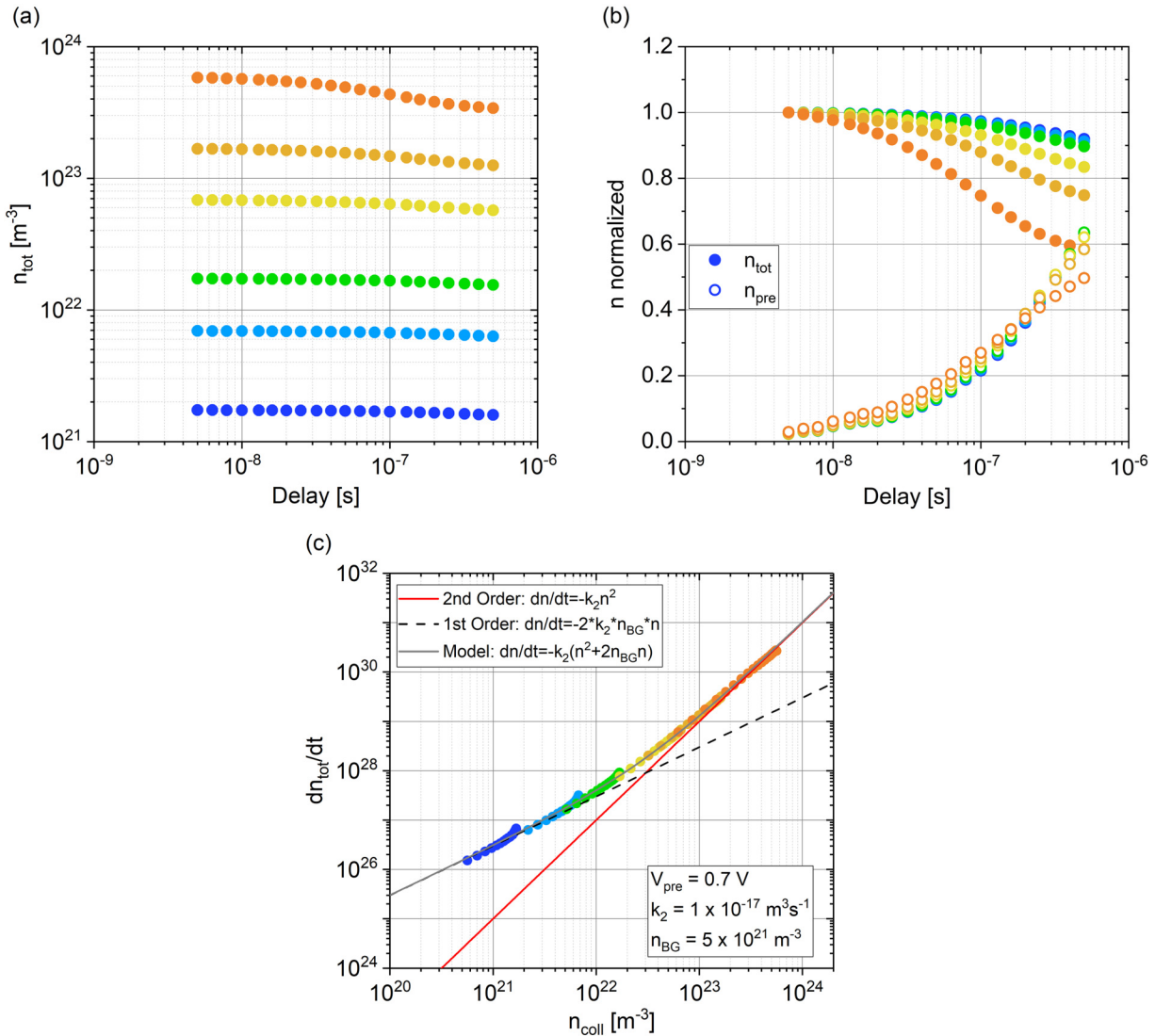


FIG. 3. (a) Simulated TDCF experiments. n_{tot} , which is the sum of the extracted charge before and after application of the collection pulse, n_{pre} and n_{coll} , respectively, as a function of the time delay between laser pulse and extraction pulse. Simulations were performed for different initial carrier densities (corresponding to the different colors in the graph). Each data point represents the integral of a simulated TDCF transient. The parameters used in this simulation were $d = 100 \text{ nm}$, $k_2 = 1 \times 10^{-17} \text{ m}^3 \text{ s}^{-1}$, $\mu_e = \mu_h = 1 \times 10^{-3} \text{ cm}^2 \text{ V}^{-1} \text{ s}^{-1}$, and no surface recombination. V_{pre} was set to 0.7 V , which is only 0.04 V below the V_{OC} at a generation rate G of $4 \times 10^{27} \text{ m}^{-3} \text{ s}^{-1}$. (b) n_{tot} and n_{pre} normalized to the initial n_{tot} (for a delay of 5 ns) as a function of the delay time. The colors of the data points correspond to the initial carrier densities shown in (a). (c) Differential carrier density decay (dn_{tot}/dt) vs collected carrier density (n_{coll}). The same color code as in (a) and (b) is used. Also shown is a fit of the high fluence data with strict second order recombination (solid red line), of the low fluence data with first order recombination (black dashed line), and of the entire data set with a model considering bimolecular recombination in the presence of a homogeneous background charge, according to Eq. (4) (solid gray line).

homogeneous, recombination-dominated carrier profiles.⁴⁵ Therefore, the data in this region can be described with a simple second order recombination model according to $dn/dt = -k_2 n^2$, where we find k_2 to be almost equal to the input value of $10^{-17} \text{ m}^3 \text{ s}^{-1}$ (solid red line). For low carrier densities, the curve is determined by recombination of photogenerated carriers with the background charge and follows a first order decay (black dashed line).

We have then fitted the entire carrier density range with Eq. (4) (solid gray line), leaving both k_2 and the background charge n_{BG} as free fit parameters. The result of the best fit is $k_2 = 0.93 \times 10^{-17} \text{ m}^3 \text{ s}^{-1}$, which is very close to the input value of $k_2 = 10^{-17} \text{ m}^3 \text{ s}^{-1}$. Note that accurate fits can only be achieved if the measured data cover a sufficiently large fluence range, which includes both limiting cases of pure first and second order. The value of n_{BG} in the fit

in Fig. 3(c) is $1.6 \times 10^{22} \text{ m}^{-3}$, and the meaning of this value will be discussed in more detail below.

1. The effect of prebias and dark charge

It has been pointed out that the accuracy of TDCF to determine the order and coefficient of NGR can be falsified by the recombination of photogenerated charges with dark-injected charges.⁴⁶ A way out of this problem may be to use a prebias much smaller than the built-in potential, but this comes at the cost of accelerated extraction during the delay. Therefore, simulations have been performed at $V_{\text{pre}} = 0.6 \text{ V}$ and $V_{\text{pre}} = 0.8 \text{ V}$, below and above the V_{OC} of the cell, with the resulting differential decay plots shown in Fig. 4. All other parameters were the same as in Fig. 3. One main difference between these cases is the distribution of the dark charge due to the different prebias conditions [compare Fig. 5(a)]. At 0.6 V , significantly less background charge is present in the device compared to 0.7 V and 0.8 V , and the distribution is very inhomogeneous. In addition, the charge displacement during delay is more significant in this case. This is also seen in Fig. S2 in the [supplementary material](#), where we plot n_{tot} and n_{pre} as a function of delay time. For $V_{\text{pre}} = 0.6 \text{ V}$, nearly 50% of the initially present charge is extracted after 100–200 ns, competing efficiently with NGR. Higher initial carrier densities give rise to a slower extraction, due to the formation of space charge as pointed out above. On the other hand, at 0.8 V the amount of background charge is strongly increased and the distribution is quite homogeneous across the layer while charge extraction at V_{pre} is slow. Despite these differences, the differential decay data can be well fitted with Eq. (4) over the entire range for either prebias, with the

fit parameters $k_2 = 0.973 \times 10^{-17} \text{ m}^3 \text{ s}^{-1}$ and $n_{\text{BG}} = 3.7 \times 10^{21} \text{ m}^{-3}$ for 0.6 V and $k_2 = 0.93 \times 10^{-17} \text{ m}^3 \text{ s}^{-1}$ and $n_{\text{BG}} = 5.3 \times 10^{22} \text{ m}^{-3}$ for 0.8 V . Again, the extracted values for k_2 are very close to the input values of the simulation. We notice, however, that the low fluence traces in the $V_{\text{pre}} = 0.6 \text{ V}$ differential decay plot display an apparent higher recombination rate at early times. This is mainly due to the initial recombination of photogenerated charges with dark-injected carriers, which rapidly slows down due to the small (and inhomogeneously distributed) dark charge at this small prebias.

We now address the question, how the extracted n_{BG} can be related to the real background charge distribution. Figure 5(a) displays the background carrier distribution for the three different prebias conditions used in Fig. 4. As expected, the carrier density in the device increases and the distribution becomes more homogeneous for increasing prebias. Figure 5(b) plots the mean electron density in the active layer, the electron density in the center, the drift-length weighted carrier density (which would be measured with dark-BACE at the particular prebias), and the value of n_{BG} gained from the fit of the TDCF recombination plots as a function of prebias. Notably, the latter ones agree very well, where the slightly higher n_{BG} from the TDCF fits can be attributed to the high carrier densities in the vicinity of the contacts that speed up recombination of the photogenerated carriers with dark charge. The best agreement is reached for the highest prebias where the distribution is the most homogeneous.

To further screen the valid parameter range of the model, simulations were then performed with higher BMR coefficients of $k_2 = 1 \times 10^{-16} \text{ m}^3 \text{ s}^{-1}$ [Fig. 6(a)] and $k_2 = 1 \times 10^{-15} \text{ m}^3 \text{ s}^{-1}$ [Fig. 6(b)], the latter corresponding to Langevin-type recombination. In a real

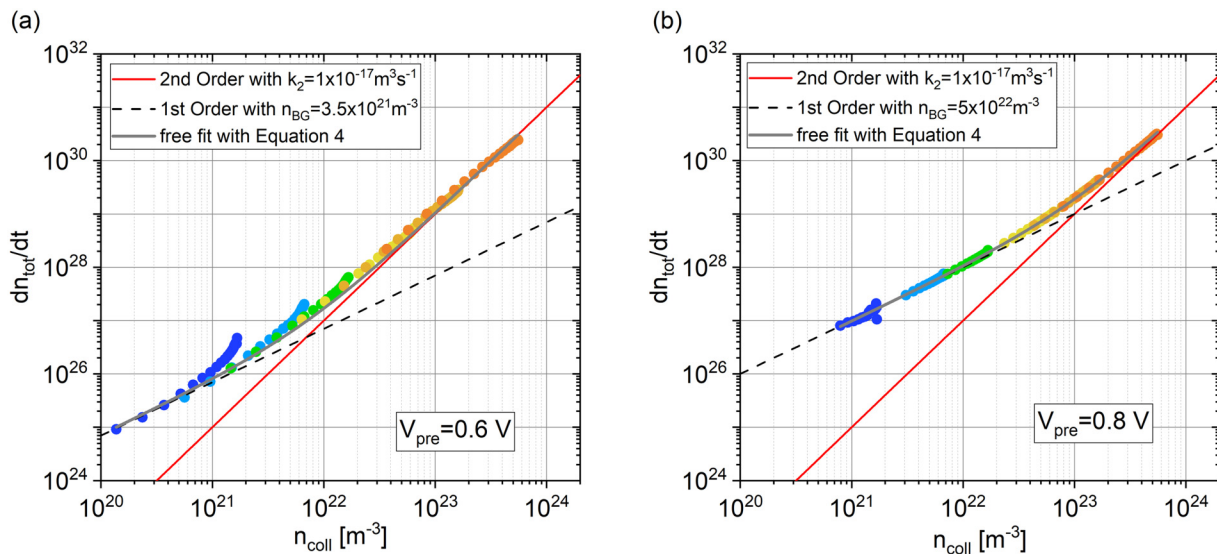


FIG. 4. Differential carrier density decay (dn_{tot}/dt) vs collected carrier density (n_{coll}) for the same device as in Fig. 3 but at different prebiases: (a) $V_{\text{pre}} = 0.6 \text{ V}$ and (b) $V_{\text{pre}} = 0.8 \text{ V}$. The red lines show strict second order recombination with the input value $k_2 = 1 \times 10^{-17} \text{ m}^3 \text{ s}^{-1}$. The black dashed lines follow a first order model with $k_2 = 1 \times 10^{-17} \text{ m}^3 \text{ s}^{-1}$ and $n_{\text{BG}} = 3.5 \times 10^{21} \text{ m}^{-3}$ in (a) and $n_{\text{BG}} = 5 \times 10^{22} \text{ m}^{-3}$ in (b). The gray lines are fits according to Eq. (4) with k_2 and n_{BG} as free fit parameters. Best fits were obtained with $k_2 = 9.73 \times 10^{-18} \text{ m}^3 \text{ s}^{-1}$ and $n_{\text{BG}} = 3.7 \times 10^{21} \text{ m}^{-3}$ in (a) and $k_2 = 9.3 \times 10^{-18} \text{ m}^3 \text{ s}^{-1}$, $n_{\text{BG}} = 5.3 \times 10^{22} \text{ m}^{-3}$ in (b).

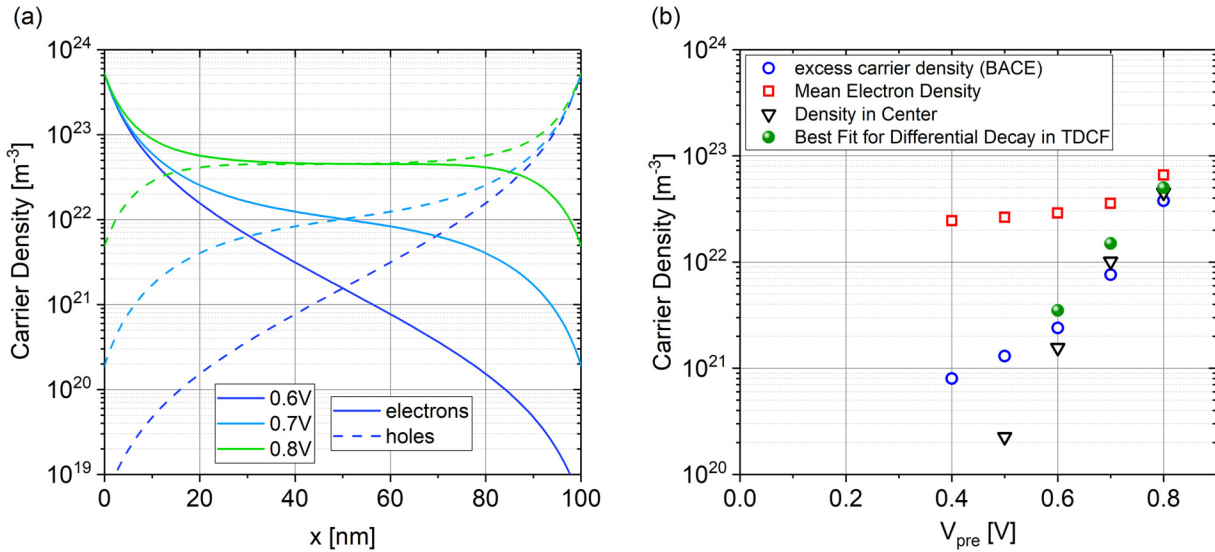


FIG. 5. (a) Simulated charge carrier density profiles in the dark for the device described in Fig. 4 at 0.6 V, 0.7 V, and 0.8 V. (b) Based on the carrier density profiles in (a), this graph displays the drift-length weighted excess carrier density as it would be measured with dark-BACE, including a correction by a reference measurement with the same voltage jump but starting at 0 V (empty blue circles), the mean electron density (empty red squares), and the carrier density in the center of the device (empty black triangles). Also shown are the values n_{BG} from the best fit for the differential decay in Figs. 3(c) and 4 (full green circles).

TDCF experiment, the collection voltage is limited by the breakdown voltage of the device and, in the case of very high recombination, it cannot be chosen high enough to avoid recombination during extraction. Therefore, for such high BMR coefficients, not all the

charges that survived recombination during the delay can be extracted by the collection pulse and n_{coll} will be in general too small. This can be seen from the lower “initially extracted” carrier densities in Fig. 6(b) compared to Fig. 6(a), despite the fact that both

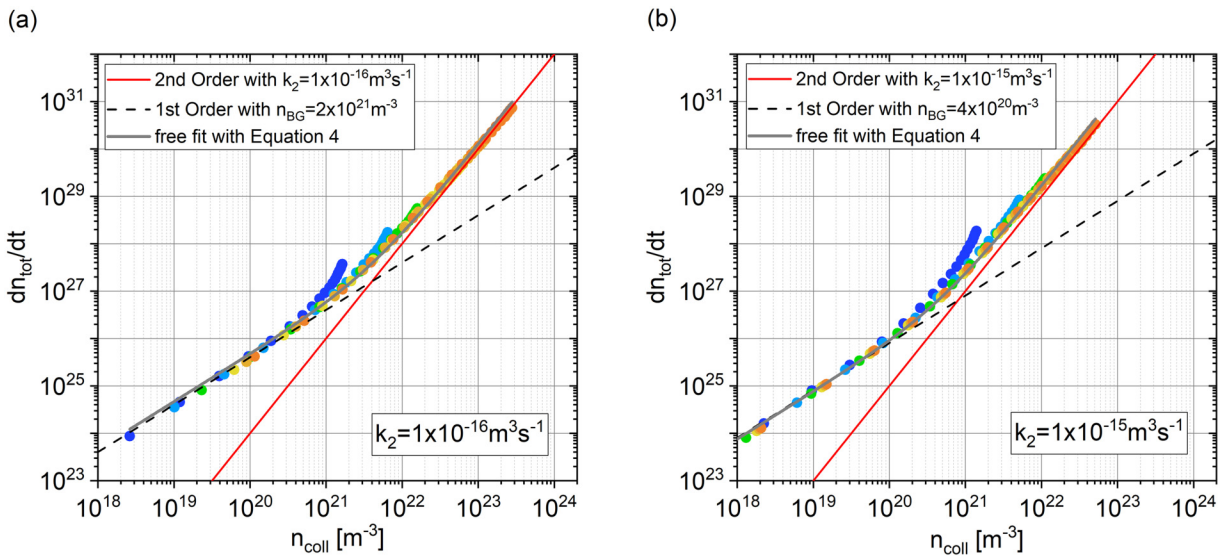


FIG. 6. Differential decay data for a 100 nm device with (a) $k_2 = 1 \times 10^{-16} \text{ m}^3 \text{ s}^{-1}$ and (b) $k_2 = 1 \times 10^{-15} \text{ m}^3 \text{ s}^{-1}$. Mobilities were $\mu_e = \mu_h = 1 \times 10^{-3} \text{ cm}^2 \text{ V}^{-1} \text{ s}^{-1}$ as before and surface recombination was turned off. The prebias was chosen to be 0.1 V lower than the V_{QC} at one sun, which is $V_{pre} = 0.58 \text{ V}$ in (a) and $V_{pre} = 0.52 \text{ V}$ in (b). The parameters from the free fits with Eq. (4) (solid gray lines) were $k_2 = 1.2 \times 10^{-16} \text{ m}^3 \text{ s}^{-1}$ and $n_{BG} = 1.9 \times 10^{21} \text{ m}^{-3}$ for (a) and $k_2 = 1.6 \times 10^{-15} \text{ m}^3 \text{ s}^{-1}$ and $n_{BG} = 2.3 \times 10^{20} \text{ m}^{-3}$ for (b).

simulations were performed with the same input parameters (except the value of k_2). Nevertheless, in both cases, the differential decay data obey Eq. (4), yielding BMR coefficients [$k_2 = 1.2 \times 10^{-16} \text{ m}^3 \text{ s}^{-1}$ in (a) and $k_2 = 1.6 \times 10^{-15} \text{ m}^3 \text{ s}^{-1}$ in (b)] close to the input values in the simulation. Also, the values for n_{BG} obtained from the fits [$1.9 \times 10^{21} \text{ m}^{-3}$ in (a) and $2.3 \times 10^{20} \text{ m}^{-3}$ in (b)] resemble the one order of magnitude difference in the BMR coefficient.

Here, we like to comment on the conclusions from the recent study by Würfel and Unmüssig on the reliability of recombination studies with TDCF.⁴⁶ Their drift-diffusion simulation showed (Figs. 4 and 5 of that work) that the determination of the (time dependent) recombination with TDCF becomes unreliable for initial carrier densities of $5 \times 10^{21} \text{ m}^{-3}$ and below. This corresponds to a fluence of ca. 20 nJ cm^{-2} and smaller, depending on the exact excitation wavelength and thickness. Our TDCF recombination studies always include measurements with fluences of hundreds of nJ cm^{-2} and more. This is to ensure that recombination is dominated by photogenerated charges. For a too low fluence (and laser induced carrier density), TDCF measurements do not provide reliable data of the charge recombination dynamics because dark-injected charges dominate the fate of the photogenerated carriers (as discussed in detail in Würfel's work). This is nicely shown in Fig. 3 of our work, where traces with initial carrier densities below $1 \times 10^{22} \text{ m}^{-3}$ lead to an apparent recombination order of 1. Therefore, it is of great importance to measure at sufficiently high carrier densities, where a clear second order decay is visible.

To conclude, BACE and TDCF provide a consistent set of data in the absence of surface recombination. The differential decay data can be consistently explained over 3 orders of magnitude with a model utilizing bimolecular recombination in the presence of a

homogeneous “effective” background carrier density. Notably, k_2 extracted from the high carrier density range in TDCF agrees exactly with the value from photo-BACE. Also, there is very little difference in the value of the background carrier density deduced from the simple fit to the low carrier density TDCF data and from dark-BACE. Clearly, the situation will change drastically in the case of dispersive recombination, which has been treated extensively in different work,^{31,42,47} and is, however, not the subject of this work.

2. The effect of surface recombination

If finite surface recombination at both contacts is implemented in the simulation (Fig. 7), features of a very fast initial decay along with an apparent high recombination order appear, in particular, in traces with lower initial carrier density. The reason for these features is the initial fast surface recombination of minority carriers at the “wrong” electrode, which is holes at the cathode and electrons at the anode. These “missing” charges will significantly contribute to the reduction of the extracted charge density, as according to Eq. (2) they have a maximum distance to the electrode through which they are collected upon application of the collection bias. As expected, the effect becomes less pronounced for increasing fluence and thicker active layers, when bulk BMR dominates the carrier loss. The reason for the fast slow-down of the carrier loss due to surface recombination lies in the fact that this process rapidly depletes the minority carrier reservoir near the electrodes, which gradually reduces the speed at which dark-injected charge recombines with photogenerated carriers. In line with this interpretation, this decay becomes steeper for thicker layers, because losses due to surface

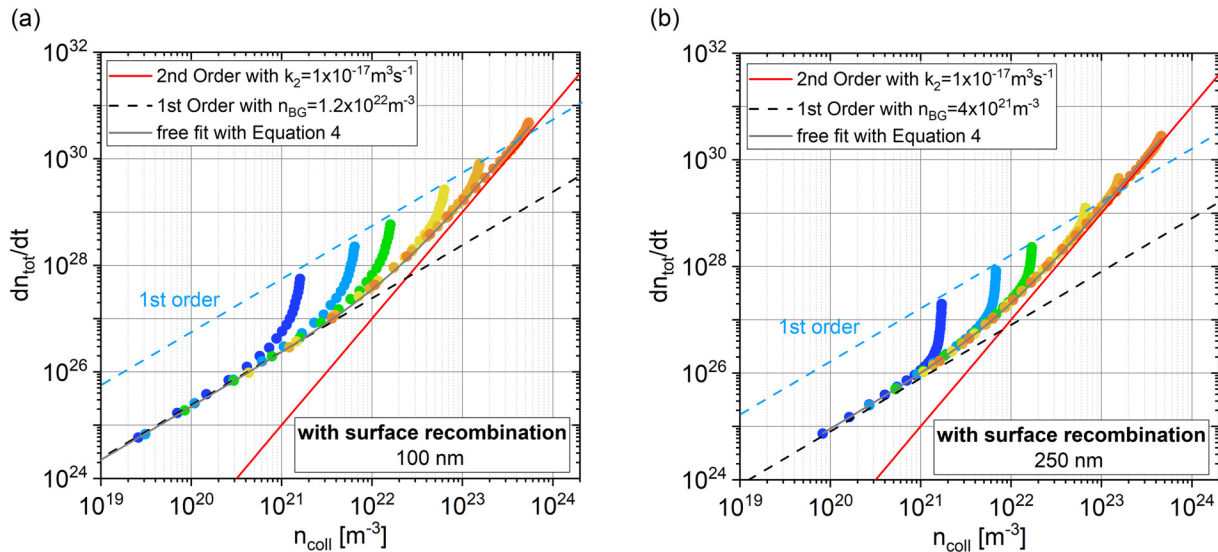


FIG. 7. Differential decay data for (a) 100 nm and (b) 250 nm device with infinite surface recombination at both contacts. The input parameters were $k_2 = 1 \times 10^{-17} \text{ m}^3 \text{ s}^{-1}$ and $\mu_e = \mu_h = 1 \times 10^{-3} \text{ cm}^2 \text{ V}^{-1} \text{ s}^{-1}$. We set $V_{\text{pre}} = 0.6 \text{ V}$ in (a) and $V_{\text{pre}} = 0.62 \text{ V}$ in (b), 0.1 V below the corresponding V_{OC} of 0.7 and 0.72 V, respectively. The solid gray lines are free fits with Eq. (4) and yield $k_2 = 1.3 \times 10^{-17} \text{ m}^3 \text{ s}^{-1}$ and $n_{\text{BG}} = 0.9 \times 10^{22} \text{ m}^{-3}$ in (a) and $k_2 = 1.15 \times 10^{-17} \text{ m}^3 \text{ s}^{-1}$ and $n_{\text{BG}} = 3.9 \times 10^{21} \text{ m}^{-3}$ in (b).

recombination of minority carriers close to the contacts contribute now only little to the overall charge carrier dynamics.

A free fit to the differential data to the long time decay data with Eq. (4b) still gives k_2 values that are very close to the input values. For a meaningful fit, it is important that the data show a clear (bulk BMR dominating) region with a slope 2. Also, the early decay data, which are clearly dominated by surface losses, have to be omitted. If these constraints are carefully considered, TDCF is a reliable method for determining BMR coefficients, even in the case of surface recombination. However, the value for n_{BG} obtained from a fit with Eq. (4) cannot be unambiguously attributed to a background charge. This is because surface recombination causes an additional first order contribution, even for low photogenerated carrier densities.

The appearance of rapid early time recombination traces in the differential decay data with surface recombination reminds of the characteristic decay pattern of dispersive recombination.⁴⁷ However, in contrast to dispersive BMR, the extra contribution from surface recombination follows a strict 1st order dependence on carrier density [see the blue dashed lines connecting the initial recombination data in Figs. 7(a) and 7(b)]. Equitemporal fits to the data sets with increasing initial carrier density give a recombination order close to 1 for all time delays (see Fig. S3 in the [supplementary material](#)), allowing to safely disentangle surface recombination from dispersive higher order recombination.

To conclude, surface recombination has a significant effect on the early time recombination data in TDCF, but this extra recombination loss decreases continuously with time. As a consequence, TDCF traces for different fluences merge to a common line, and the analysis of this line with Eq. (4) yields the correct value for k_2 . BACE, on the other hand, yields a significantly higher recombination rate and apparent BMR coefficient. Therefore, surface recombination should become apparent when comparing the results from these two techniques.

IV. COMPARISON WITH EXPERIMENTAL DATA

Figure 8 shows the results of a combined TDCF/BACE study of a device with a 100 nm thick blend of the donor polymer PM6 with the nonfullerene acceptor Y6 (see Ref. 1 for the full names and chemical structure of the compounds). This material combination gives solar cells with power conversion efficiencies above 15% for rather thin devices (150 nm and below), while thicker devices suffer from a continuous drop of the fill factor (FF)—indicative of significant nongeminate losses. TDCF was measured with different initial fluences and at three different prebias voltages. We notice a weak early time slow-down of the recombination rate for some of the low fluence traces. While this observation may hint at an initial carrier loss due to surface recombination or recombination of photogenerated with dark-injected charge as pointed out above, there is no clear correlation with prebias. The $R(n)$ data then quickly merge to a common line, which has a slope of 2 for high carrier densities, indicating that bimolecular recombination is the dominating recombination process in this blend. To fit the data with Eq. (4), we determined the dark background charge density n_{BG} at each prebias, using dark-BACE. As expected, increasing the prebias V_{pre} toward V_{OC} goes along with a pronounced increase of n_{BG} . Despite the large variation of the bias condition, all data can be

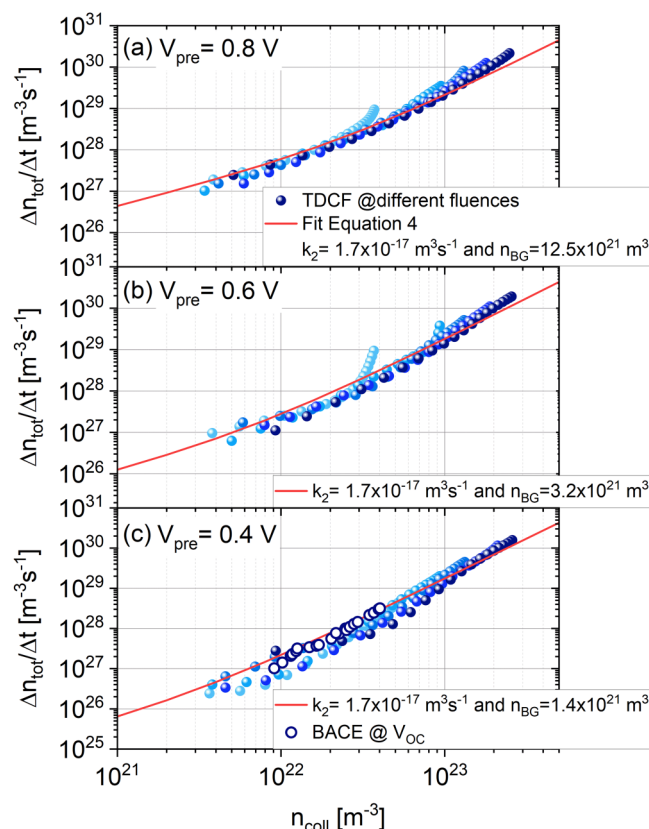


FIG. 8. TDCF differential decay data (solid circles) of a device with a 100 nm thick PM6:Y6 blend, measured at different fluences (between 0.2 and $4 \mu\text{J cm}^{-2}$) and different prebias voltages. (a) $V_{pre} = 0.8 \text{ V}$, (b) $V_{pre} = 0.6 \text{ V}$, and (c) $V_{pre} = 0.4 \text{ V}$ (compared to a V_{OC} of 0.84 V under simulated AM1.5G conditions). The solid red lines are fits to Eq. (4) with the fit parameters k_2 and n_{BG} (measured by dark-BACE) as denoted in the graph. The empty circles in panel (c) are BACE data measured under illumination at V_{OC} .

consistently fitted by a strict bimolecular recombination process, yielding a bias- and intensity-independent BMR coefficient $k_2 = 1.7 \times 10^{-17} \text{ m}^3 \text{ s}^{-1}$. These findings are in perfect agreement with the prediction from the simulations above in the absence of surface recombination. We note that recent impedance spectroscopy study on PM6:Y6 reported a k_2 of $3\text{--}5.8 \times 10^{-19} \text{ m}^3 \text{ s}^{-1}$.⁴⁸ These measurements were performed on a regular device geometry, with a PEDOT:PSS bottom electrode. Therefore, the lower k_2 reported in Ref. 48 may result from a specific blend morphology due to a different bottom electrode. Also plotted in Fig. 8(c) is the result of steady state recombination measurements with BACE (open circles) on the same sample. The measurement was performed with increasing steady state illumination intensity at the respective V_{OC} where the generation rate G is equal to the recombination rate R . Therefore, the BACE data can be plotted together with the differential decay data from TDCF. It is remarkable how well the steady state data match the transient data, even though the conditions for both

measurements are distinctly different. We conclude that the nongenerated loss in this thin high-performance blend is entirely determined by a second order recombination process in the bulk and that surface recombination is of minor importance.

V. DISCUSSION AND CONCLUSION

By performing 1D drift-diffusion simulations of BACE and TDCF experiments, we examine the applicability of the two methods to determine the order of recombination and the BMR coefficient for a wide range of parameters, with and without surface recombination.

If surface recombination is excluded, BACE measurements yield accurate values for the recombination order and coefficient, provided that the illumination intensity (photogenerated carrier density) is sufficiently high. Under these conditions, the total (injected and photogenerated) carrier profiles are fairly homogeneous except in the direct vicinity of the electrodes. As expected and reported earlier, decreasing the active layer thickness causes deviations from the predicted BMR behavior, in particular, at low carrier densities.

TDCF, on the other hand, reveals highly reliable values for k_2 , irrespective of the layer thickness, prebias, and BMR coefficient. This has two main reasons. First, the carrier profiles of the photogenerated electrons and holes are initially the same, and they are more homogeneous than the steady state profiles. Second, TDCF allows higher carrier densities to be generated, thereby reducing the effect of dark-injected carriers on recombination. This conclusion holds even for the case of high BMR coefficients, where photogenerated charges recombine during extraction. Interestingly, the functional dependence of the excess recombination rate R as a function of excess carrier density can be exactly reproduced with a simple model which assumes a homogeneous background density, and this background density is (within a factor of 2) identical to the carrier density deduced from dark-BACE experiments. Therefore, while TDCF provides accurate values for k_2 if measurements are performed over a wide enough fluence range, BACE is a well-suited complementary technique to confirm the results from the fitting of the TDCF data. In previous experimental work, BACE and TDCF results could be consistently explained with the very same set of parameters.^{28,35}

The situation changes drastically if surface recombination comes into play. In this case, recombination properties as deduced from BACE measurements do not, anymore, represent the bulk properties. This is because of the extra recombination loss at the electrodes and the concurrent reduction in carrier density near the contacts. It is only at high bulk recombination rates that BACE measurements provide accurate numbers. Importantly, if BACE measurements are performed for only one thickness, it is very difficult to distinguish between bulk and surface recombination, e.g., to decide whether an apparent high k_2 is due to fast bulk recombination or it comes from additional surface recombination.

Fortunately, TDCF is suited to differentiate between these two effects. In a transient experiment, surface recombination is strongest at early times, while bulk recombination (either between photogenerated carriers or between photogenerated and dark-injected carriers) proceeds throughout the entire time range. This is nicely

reproduced by the fast early time recombination in Fig. 7, which remains of first order in carrier density during the entire time period but slows down rapidly, finally converting to a common $R(n)$ dependence. Notably, the final $R(n)$ dependence is again consistent with Eq. (4), and it allows one to obtain accurate values for k_2 if experiments can be performed up to fairly high fluences.

SUPPLEMENTARY MATERIAL

See the [supplementary material](#) for exemplary charge carrier density profiles, TDCF carrier densities at two more prebias values, and equitemporal fits to the differential decay data in the presence of surface recombination.

ACKNOWLEDGMENTS

This work is part of the interconnecting project UNVEIL (supported by the German Ministry of Science and Education, Funding Reference No. FKZ 13N13719) and of the research program of the Foundation for Fundamental Research on Matter (FOM), which is part of the Netherlands Organization for Scientific Research (NWO). The work was further supported by a grant from STW/NWO (No. VIDI 13476). Y. Zou acknowledges the National Natural Science Foundation of China (NNSFC) (No. 21875286). This is a publication by the FOM Focus Group "Next Generation Organic Photovoltaics," participating in the Dutch Institute for Fundamental Energy Research (DIFFER).

REFERENCES

- ¹J. Yuan, Y. Zhang, L. Zhou, G. Zhang, H.-L. Yip, T.-K. Lau, X. Lu, C. Zhu, H. Peng, P. A. Johnson *et al.*, "Single-Junction organic solar cell with over 15% efficiency using fused-ring acceptor with electron-deficient core," *Joule* **3**, 1140–1151 (2019).
- ²Y. Cui, H. Yao, J. Zhang, T. Zhang, Y. Wang, L. Hong, K. Xian, B. Xu, S. Zhang, J. Peng *et al.*, "Over 16% efficiency organic photovoltaic cells enabled by a chlorinated acceptor with increased open-circuit voltages," *Nat. Commun.* **10**, 2515 (2019).
- ³X. Xu, K. Feng, Z. Bi, W. Ma, G. Zhang, and Q. Peng, "Single-junction polymer solar cells with 16.35% efficiency enabled by a platinum(II) complexation strategy," *Adv. Mater.* **31**, 1901872 (2019).
- ⁴C. M. Proctor, M. Kuik, and T.-Q. Nguyen, "Charge carrier recombination in organic solar cells," *Prog. Polym. Sci.* **38**, 1941–1960 (2013).
- ⁵M. Stolterfoht, A. Armin, B. Philippa, R. D. White, P. L. Burn, P. Meredith, G. Juška, and A. Pivrikas, "Photocarrier drift distance in organic solar cells and photodetectors," *Sci. Rep.* **5**, 9949 (2015).
- ⁶D. Bartsaghi, I. d. C. Pérez, J. Kniepert, S. Roland, M. Turbiez, D. Neher, and L. J. A. Koster, "Competition between recombination and extraction of free charges determines the fill factor of organic solar cells," *Nat. Commun.* **6**, 7083 (2015).
- ⁷D. Neher, J. Kniepert, A. Elimelech, and L. J. A. Koster, "A new figure of merit for organic solar cells with transport-limited photocurrents," *Sci. Rep.* **6**, 24861 (2016).
- ⁸P. Kaienburg, U. Rau, and T. Kirchartz, "Extracting information about the electronic quality of organic solar-cell absorbers from fill factor and thickness," *Phys. Rev. Appl.* **6**, 024001 (2016).
- ⁹S. Shoaee, M. Stolterfoht, and D. Neher, "The role of mobility on charge generation, recombination, and extraction in polymer-based solar cells," *Adv. Energy Mater.* **8**, 1703355 (2018).

- ¹⁰C. G. Shuttle, B. O'Regan, A. M. Ballantyne, J. Nelson, D. D. C. Bradley, and J. R. Durrant, "Bimolecular recombination losses in polythiophene:fullerene solar cells," *Phys. Rev. B Condens. Matter Mater. Phys.* **78**, 113201 (2008).
- ¹¹J. Guo, H. Ohkita, S. Yokoya, H. Bente, and S. Ito, "Bimodal polarons and hole transport in poly(3-hexylthiophene):Fullerene blend films," *J. Am. Chem. Soc.* **132**, 9631–9637 (2010).
- ¹²S. M. Menke, A. Sadhanala, M. Nikolka, N. A. Ran, M. K. Ravva, S. Abdel-Azeim, H. L. Stern, M. Wang, H. Sirringhaus, T.-Q. Nguyen *et al.*, "Limits for recombination in a low energy loss organic heterojunction," *ACS Nano* **10**, 10736–10744 (2016).
- ¹³L. M. Andersson, A. Melianas, Y. Infahsaeng, Z. Tang, A. Yartsev, O. Inganäs, and V. Sundström, "Unified study of recombination in polymer:fullerene solar cells using transient absorption and charge-extraction measurements," *J. Phys. Chem. Lett.* **4**, 2069–2072 (2013).
- ¹⁴A. J. Mozer, N. S. Sariciftci, L. Lutsen, D. Vanderzande, R. Österbacka, M. Westerling, and G. Juška, "Charge transport and recombination in bulk heterojunction solar cells studied by the photoinduced charge extraction in linearly increasing voltage technique," *Appl. Phys. Lett.* **86**, 112104 (2005).
- ¹⁵N. Gasparini, M. Salvador, T. Heumüller, M. Richter, A. Classen, S. Shrestha, G. J. Matt, S. Holliday, S. Strohm, H.-J. Egelhaaf *et al.*, "Polymer:nonfullerene bulk heterojunction solar cells with exceptionally low recombination rates," *Adv. Energy Mater.* **7**, 1701561 (2017).
- ¹⁶C. G. Shuttle, B. O'Regan, A. M. Ballantyne, J. Nelson, D. D. C. Bradley, J. De Mello, and J. R. Durrant, "Experimental determination of the rate law for charge carrier decay in a polythiophene:fullerene solar cell," *Appl. Phys. Lett.* **92**, 093311 (2008).
- ¹⁷R. Hamilton, C. G. Shuttle, B. O'Regan, T. C. Hamman, J. Nelson, and J. R. Durrant, "Recombination in annealed and nonannealed polythiophene/fullerene solar cells: Transient photovoltage studies versus numerical modeling," *J. Phys. Chem. Lett.* **1**, 1432–1436 (2010).
- ¹⁸D. Baran, N. Gasparini, A. Wadsworth, C. H. Tan, N. Wehbe, X. Song, Z. Hamid, W. Zhang, M. Neophytou, T. Kirchartz *et al.*, "Robust nonfullerene solar cells approaching unity external quantum efficiency enabled by suppression of geminate recombination," *Nat. Commun.* **9**, 2059 (2018).
- ¹⁹D. Kiermasch, A. Baumann, M. Fischer, V. Dyakonov, and K. Tvingstedt, "Revisiting lifetimes from transient electrical characterization of thin film solar cells: A capacitive concern evaluated for silicon, organic and perovskite devices," *Energy Environ. Sci.* **11**, 629–640 (2018).
- ²⁰O. J. Sandberg, K. Tvingstedt, P. Meredith, and A. Armin, "Theoretical perspective on transient photovoltage and charge extraction techniques," *J. Phys. Chem. C* **123**, 14261–14271 (2019).
- ²¹C. G. Shuttle, A. Maurano, R. Hamilton, B. O'Regan, J. C. De Mello, and J. R. Durrant, "Charge extraction analysis of charge carrier densities in a polythiophene/fullerene solar cell: Analysis of the origin of the device dark current," *Appl. Phys. Lett.* **93**, 183501 (2008).
- ²²C. M. Proctor, C. Kim, D. Neher, and T. Q. Nguyen, "Nongeminate recombination and charge transport limitations in diketopyrrolopyrrole-based solution-processed small molecule solar cells," *Adv. Funct. Mater.* **23**, 3584–3594 (2013).
- ²³C. Deibel, A. Wagenpahl, and V. Dyakonov, "Origin of reduced polaron recombination in organic semiconductor devices," *Phys. Rev. B Condens. Matter Mater. Phys.* **80**, 075203 (2009).
- ²⁴T. Kirchartz and J. Nelson, "Meaning of reaction orders in polymer:fullerene solar cells," *Phys. Rev. B* **86**, 165201 (2012).
- ²⁵F. Deledalle, P. Shakya Tuladhar, J. Nelson, J. R. Durrant, and T. Kirchartz, "Understanding the apparent charge density dependence of mobility and lifetime in organic bulk heterojunction solar cells," *J. Phys. Chem. C* **118**, 8837–8842 (2014).
- ²⁶A. Spies, M. List, T. Sarkar, and U. Würfel, "On the impact of contact selectivity and charge transport on the open-circuit voltage of organic solar cells," *Adv. Energy Mater.* **7**, 1601750 (2017).
- ²⁷J. Kniepert, M. Schubert, J. C. Blakesley, and D. Neher, "Photogeneration and recombination in P3HT/PCBM solar cells probed by time-delayed collection field experiments," *J. Phys. Chem. Lett.* **2**, 700–705 (2011).
- ²⁸J. Kniepert, I. Lange, N. J. van der Kaap, L. J. A. Koster, and D. Neher, "A conclusive view on charge generation, recombination, and extraction in As-prepared and annealed P3HT:PCBM blends: Combined experimental and simulation work," *Adv. Energy Mater.* **4**, 1301401 (2014).
- ²⁹S. Albrecht, S. Janietz, W. Schindler, J. Frisch, J. Kurpiers, J. Kniepert, S. Inal, P. Pingel, K. Fostiropoulos, N. Koch *et al.*, "Fluorinated copolymer PCPDTBT with enhanced open-circuit voltage and reduced recombination for highly efficient polymer solar cells," *J. Am. Chem. Soc.* **134**, 14932 (2012).
- ³⁰W. Li, S. Albrecht, L. Yang, S. Roland, J. R. Tumbleston, T. McAfee, L. Yan, M. A. Kelly, H. Ade, D. Neher *et al.*, "Mobility-Controlled performance of thick solar cells based on fluorinated copolymers," *J. Am. Chem. Soc.* **136**, 15566–15576 (2014).
- ³¹J. Kurpiers and D. Neher, "Dispersive Non-geminate recombination in an amorphous polymer:fullerene blend," *Sci. Rep.* **6**, 26832 (2016).
- ³²S. Roland, L. Yan, Q. Zhang, X. Jiao, A. Hunt, M. Ghasemi, H. Ade, W. You, and D. Neher, "Charge generation and mobility-limited performance of bulk heterojunction solar cells with a higher adduct fullerene," *J. Phys. Chem. C* **121**, 10305–10316 (2017).
- ³³S. M. Hosseini, S. Roland, J. Kurpiers, Z. Chen, K. Zhang, F. Huang, A. Armin, D. Neher, and S. Shoaee, "Impact of bimolecular recombination on the fill factor of fullerene and nonfullerene-based solar cells: A comparative study of charge generation and extraction," *J. Phys. Chem. C* **123**, 6823–6830 (2019).
- ³⁴T. Ferron, M. Waldrip, M. Pope, and B. A. Collins, "Increased charge transfer state separation via reduced mixed phase interface in polymer solar cells," *J. Mater. Chem. A* **7**, 4536–4548 (2019).
- ³⁵J. Kniepert, I. Lange, J. Heidbrink, J. Kurpiers, T. J. K. Brenner, L. J. A. Koster, and D. Neher, "Effect of solvent additive on generation, recombination, and extraction in PTB7:PCBM solar cells: A conclusive experimental and numerical simulation study," *J. Phys. Chem. C* **119**, 8310–8320 (2015).
- ³⁶L. J. A. Koster, E. C. P. Smits, V. D. Mihaileti, and P. W. M. Blom, "Device model for the operation of polymer/fullerene bulk heterojunction solar cells," *Phys. Rev. B* **72**, 085205 (2005).
- ³⁷V. M. Le Corre, A. R. Chatri, N. Y. Doumon, and L. J. A. Koster, "Charge carrier extraction in organic solar cells governed by steady-state mobilities," *Adv. Energy Mater.* **7**, 1701138 (2017).
- ³⁸A. Rahimi Chatri, S. Torabi, V. M. Le Corre, and L. J. A. Koster, "Impact of electrodes on recombination in bulk heterojunction organic solar cells," *ACS Appl. Mater. Interfaces* **10**, 12013–12020 (2018).
- ³⁹U. Würfel, L. Perdígón-Toro, J. Kurpiers, C. M. Wolff, P. Caprioglio, J. J. Rech, J. Zhu, X. Zhan, W. You, S. Shoaee *et al.*, "Recombination between photogenerated and electrode-induced charges dominates the fill factor losses in optimized organic solar cells," *J. Phys. Chem. Lett.* **10**, 3473–3480 (2019).
- ⁴⁰S. A. Hawks, B. Y. Finck, and B. J. Schwartz, "Theory of current transients in planar semiconductor devices: Insights and applications to organic solar cells," *Phys. Rev. Appl.* **3**, 044014 (2015).
- ⁴¹D. Rauh, C. Deibel, and V. Dyakonov, "Charge density dependent nongeminate recombination in organic bulk heterojunction solar cells," *Adv. Funct. Mater.* **22**, 3371–3377 (2012).
- ⁴²A. Hofacker and D. Neher, "Dispersive and steady-state recombination in organic disordered semiconductors," *Phys. Rev. B* **96**, 245204 (2017).
- ⁴³O. J. Sandberg, A. Sundqvist, M. Nyman, and R. Österbacka, "Relating charge transport, contact properties, and recombination to open-circuit voltage in sandwich-type thin-film solar cells," *Phys. Rev. Appl.* **5**, 044005 (2016).
- ⁴⁴J. Kurpiers, T. Ferron, S. Roland, M. Jakoby, T. Thiede, F. Jaiser, S. Albrecht, S. Janietz, B. A. Collins, I. A. Howard *et al.*, "Probing the pathways of free charge generation in organic bulk heterojunction solar cells," *Nat. Commun.* **9**, 2038 (2018).
- ⁴⁵A. Pivrikas, G. Juška, A. J. Mozer, M. Scharber, K. Arlauskas, N. S. Sariciftci, H. Stubb, and R. Österbacka, "Bimolecular recombination coefficient as a sensitive testing parameter for low-mobility solar-cell materials," *Phys. Rev. Lett.* **94**, 176806 (2005).

⁴⁶U. Würfel and M. Unmüssig, “Apparent field-dependence of the charge carrier generation in organic solar cells as a result of (bimolecular) recombination,” *Sol. RRL* **2**, 1800229 (2018).

⁴⁷S. Roland, J. Kniepert, J. A. Love, V. Negi, F. Liu, P. Bobbert, A. Melianas, M. Kemerink, A. Hofacker, and D. Neher, “Equilibrated charge carrier populations govern steady-state nongeminate recombination in

disordered organic solar cells,” *J. Phys. Chem. Lett.* **10**, 1374–1381 (2019).

⁴⁸A. Karki, J. Vollbrecht, A. L. Dixon, N. Schopp, M. Schrock, G. N. M. Reddy, and T. Nguyen, “Understanding the high performance of over 15% efficiency in single-junction bulk heterojunction organic solar cells,” *Adv. Mater.* (published online).